Applied Physics A (2021) 127:818
https://doi.org/10.1007/s00339-021-04964-1

Applied Physics A
Materials Science & Processing

Preparation and photocatalytic properties of ZnO nanorods/g-C_3N_4 composite

Fucheng Yu[1] · Yuanmeng Li[1] · Zhengyan Liu[1] · Dongmei Nan[1] · Bolong Wang[1] · Ling He[1] · Jianbin Zhang[1] · Xianxi Tang[1] · Yangshuo Liu[2]

Received: 4 April 2021 / Accepted: 26 September 2021 / Published online: 5 October 2021

Abstract
ZnO nanorods/g-C_3N_4 photocatalytic composite was prepared, and its structural and optical properties have been studied. Bulk graphite phase carbon nitride (g-C_3N_4) was first prepared by a one-step thermal polymerization method, and ZnO nanorods were grown from the ZnO seed particles on the surface of g-C_3N_4 by a hydrothermal method. The effects of hydrothermal reaction time on the morphology and photocatalytic properties of ZnO nanorods/g-C_3N_4 composite were investigated. The hydrothermal reaction included two stages. The initial stage was dominated by the rapid deposition of Zn^{2+} precursor in hydrothermal solution on ZnO seed particles to form ZnO seed layer, and the second stage was the hydrothermal growth of ZnO nanorods from the ZnO seed layer. In the second stage, two processes occurred simultaneously, namely, the dissolution of seed layer and the growth of ZnO nanorods. Hence, the composite prepared with different hydrothermal time shows different photocatalytic degradation mechanism to methyl orange (MO) solution. The photocatalytic performance of the composite sample with the grown time of 2 h is mainly attributed to separation efficiency of photogenerated carriers. For the composite sample with the grown time of 3 h, due to the partial dissolution of seed layer, its photocatalytic performance is mainly attributed to the surface reaction of ZnO nanorods. For the composite samples with the hydrothermal grown time of 4 and 5 h, the dense ZnO nanorods on the surface of g-C_3N_4 improve the separation efficiency of the photogenerated carriers, and their photocatalytic performance is attributed to both carrier lifetime and surface reaction. As a result of synergy, the sample with the hydrothermal grown time of 3 h shows the best photocatalytic performance in all composite sample.

Keywords ZnO nanorods · g-C_3N_4 composites · Hydrothermal · Photocatalysis

1 Introduction

With the aggravation of global energy crisis and environmental problems, new strategic technologies are urgently needed which can not only utilize environmentally friendly renewable energy, but also solve environmental problems in the world [1, 2]. Solar energy is a kind of rich, permanent and green energy, which is considered as the most ideal new green energy. Therefore, using solar energy to solve environmental problems has become a research hotspot in recent years. In this context, as one of the effective methods to solve the problems, semiconductor photocatalysis technology has attracted great attention [3–5]. Semiconductor photocatalysis technology is the use of semiconductor materials to activate the surface energy under the excitation of sunlight, which can be efficiently used in the catalytic synthesis of organic fuels, degradation of organic pollutants, reduction of heavy metal ions, disinfection and sterilization and other fields. It is important that photocatalytic technology can react at room temperature, which is economical and efficient. In addition, the photocatalytic material itself must be non-toxic, harmless, pollution-free and high reuse rate. In the photocatalytic treatment of pollutants, organic pollutants can be directly degraded into water and inorganic ions, and will not produce secondary pollution. It has the incomparable advantages of traditional treatment technology and is a widely used environmental treatment technology.

✉ Fucheng Yu
yufc72@163.com

[1] School of Material Science and Engineering, Lanzhou University of Technology, Lanzhou 730050, People's Republic of China

[2] Hubei Key Laboratory of Biomass Fibers and Eco-Dyeing and Finishing, Wuhan Textile University, Wuhan 430073, People's Republic of China

In recent years, the research field of photocatalytic technology is more and more extensive, such as water photolysis, biomedicine and so on. In order to perform the real use of photocatalysis technology to solve environmental problems, three important characteristics of photocatalyst need to be further studied, namely, high visible light absorption, low carrier recombination and strong surface reaction [6]. Then the preparation of high performance photocatalyst has become an urgent problem in current photocatalysis technology researches.

g-C_3N_4 was first reported in 2009 [7, 8]. As a kind of semiconductor material with nonmetallic visible light response, it has become research hotspots in the fields of energy, catalysis, sensor and energy storage material in recent years. g-C_3N_4 can be prepared directly by thermal polymerization of nitrogen rich raw materials, such as monocyanamide, dicyandiamide, melamine, urea and thiourea [9]. As an n-type semiconductor of two-dimensional layered conjugated polymer, it is non-toxic, environmentally friendly material, low cost, relatively narrow bandgap and high physical and chemical stability [10]. In addition, the high visible light absorption due to the narrow bandgap (2.70 eV) makes it one of the most potential photocatalytic materials[11]. However, the small specific surface area, insufficient light absorption, rapid recombination of electron–hole pairs and low carrier mobility restrict its catalytic performance [7, 12]. To overcome the shortcomings of g-C_3N_4 in photocatalysis, a variety of morphology modifications on it have first been carried out by researchers.

g-C_3N_4 with hollow porous prismatic structure has been designed [13]. The improvement of photocatalytic performance is attributed to larger specific surface area, more negative conduction band potential and faster carrier separation efficiency. Three-dimensional network structure g-C_3N_4 assembled by nanorods has large specific surface area and faster charge carrier transfer kinetics, which significantly improves its photocatalytic performance [14]. Nanoporous g-C_3N_4 microspheres have a high-density nanoporous structure, which can not only significantly inhibit the recombination of photogenerated carriers, but also accelerate the charge transfer between layers in g-C_3N_4[15]. Element doping in g-C_3N_4 crystal [14, 15] or noble metal decoration on its surface [16] have also been studied, which have effectively improved its photocatalytic performance. It is worth noting that there were more and more reports on photocatalytic degradation of g-C_3N_4-based composites to pollutants in recent years, such as Fe_3O_4/g-C_3N_4[17], CdS/g-C_3N_4[18] and g-C_3N_4/Cu_2O heterojunction [19]. The g-C_3N_4 composites with different semiconductors not only contribute to the rapid separation of photogenerated electron–hole pairs, but also enhance the carrier mobility in the crystals. Furthermore, the matched band structures between g-C_3N_4 and semiconductors in composites can also broaden the absorption band of sunlight [12, 13, 20]. ZnO with excellent photoelectric properties, is one of the semiconductor materials matching the band structure of g-C_3N_4, and the composite of ZnO and g-C_3N_4 has also been widely studied in photocatalysis [21]. Commonly, the composite was prepared by heat treatment method. However, there were still some unsatisfactory aspects in the ZnO/g-C_3N_4 composite prepared by this method, like single morphology, large ZnO grain size, small specific surface area and low reaction sites, which led to the low carrier transfer efficiency in composite [22, 23]. Due to the wide bandgap of ZnO of 3.37 eV, the composite of ZnO and g-C_3N_4 can broaden the absorption band from visible region to UV region [24, 25].

Based on the above discussions, a composite of ZnO nanorods/g-C_3N_4 with specific morphology was prepared by a hydrothermal method and its photocatalytic properties were studied. Differing from general method that g-C_3N_4 nanostructure grown on ZnO nanorods, bulk g-C_3N_4 as the matrix in composite was first prepared by a thermal polymerization method, and then ZnO nanorods were second grown on the surface of g-C_3N_4 by a hydrothermal method. The synthesis and photocatalytic properties of ZnO/g-C_3N_4 composites were studied from a new perspective.

2 Experimental details

2.1 *Preparation of bulk g-C_3N_4*

Bulk g-C_3N_4 was synthesized by the one-step thermal polymerization method. 1 g melamine was heated to 590 °C in an air atmosphere and kept in an alumina crucible for 4 h in an alumina crucible, then the product was grinded into powder. After washing with ethanol and deionized water (DI) in turn, the powder product was dried in vacuum drying oven at 70 °C. Finally, the yellow powder g-C_3N_4 was obtained and labeled as "CN".

2.2 Deposition of ZnO seed particles on the surface of bulk g-C_3N_4

6.585 g zinc acetate dihydrate [Zn $(CH_3COO)_2$•$2H_2O$] was dissolved in the mixed solution of 48 mL 2-methoxyethanol ($CH_3CHOHCH_2OCH_3$) and 2 mL ethanolamine (C_2H_7NO) and stirred at 70 °C for 2 h in a water bath, then the sol solution as ZnO precursor was obtained after standing for 48 h. Then 0.2 g g-C_3N_4 and 1 mL sol solution were mixed and transferred to an alumina crucible, heated at 590 °C for 1 h in an air atmosphere, and the bulk g-C_3N_4 with ZnO seed particles on its surface was obtained, labeled as "ZCN".

2.3 Growing ZnO nanorods on the surface of g-C_3N_4

0.6585 g zinc acetate dihydrate [Zn $(CH_3COO)_2 \bullet 2H_2O$], 0.42 g hexamethylenetetramine ($C_6H_{12}N_4$) and 0.48 g polyethyleneimine [(CH_2CH_2NH) n] were put into 100 mL DI water and ultrasonic dispersed for 30 min, then the hydrothermal precursor was obtained. Four samples of 0.04 g Z/CN were dispersed into the hydrothermal precursor and kept in Teflon-lined stainless autoclave at 95 °C for 2 h, 3 h, 4 h and 5 h, respectively. According to the different growth time, the four final composite samples were named as "ZO/CN-2", "ZO/CN-3", "ZO/CN-4" and "ZO/CN-5", respectively. The simplified experimental flowchart of ZO/CN series samples is illustrated in Fig. 1.

2.4 Photocatalysis experiments and experimental instruments

The photocatalytic experiments were carried out under Xe lamp simulating sunlight, and the rated power, current and voltage of the Xe lamp (CEL-LAX500, CEAULICHT) were 500 W, 20 A and 20 V, respectively, without filter. The distance between the Xe lamp and the MO solution surface was 15 cm. 0.2 g composite sample was ultrasonically dispersed into a cuvette (1 cm × 1 cm × 5 cm) containing 3.5 mL 20 mg/L MO solution. Then an UV–Vis absorption spectrometer was used to detect the absorbance change of the MO solution every 5 min. The absorbance value corresponding to the maximum absorption wavelength of MO at 465 nm was used to represent the concentration to characterize the photocatalytic performance of the sample. During the photocatalytic process, the powder sample was deposited on the bottom of the cuvette. There is no temperature monitoring and detection in the photocatalytic process.

The calculation formula of the sample degradation efficiency (η) to MO solution is [20]:

$$\eta = \left(C_0 - C\right)/C_0 \times 100\% \quad (1)$$

where "C_0" is the initial MO solution concentration and "C" is the concentration at the time "t". In addition, to investigate the active groups during the photocatalytic process, the scavengers of triethanolamine (TEOA), isopropyl alcohol (IPA) and benzoquinone (BZQ) were selected to add to the reaction system under the same experiment conditions, respectively.

The structural properties of the samples (crystallinity and phase) were examined by an X-ray diffractometer (XRD, D8 Advance, Bruker) with Bragg–Brentano geometry. The surface morphology of the samples was characterized with a cold field-emission scanning electron microscope (FESEM, JSM-6700F, JEOL) and a transmission electron microscope (TEM, JEM-2010, JEOL), the element composition of the samples was analyzed with an energy-dispersive X-ray spectrometer (EDXS) attached to the FESEM above, the optical properties of the samples were studied by a Fluorescence spectrophotometer (PL, F97 pro, Lengguang Technology) with wavelength of 300 nm, the specific parameters are as follows: xenon lamp source, AC 220 V, frequency 50 Hz, rated power 200 W, sample carrier is a rectangular iron block

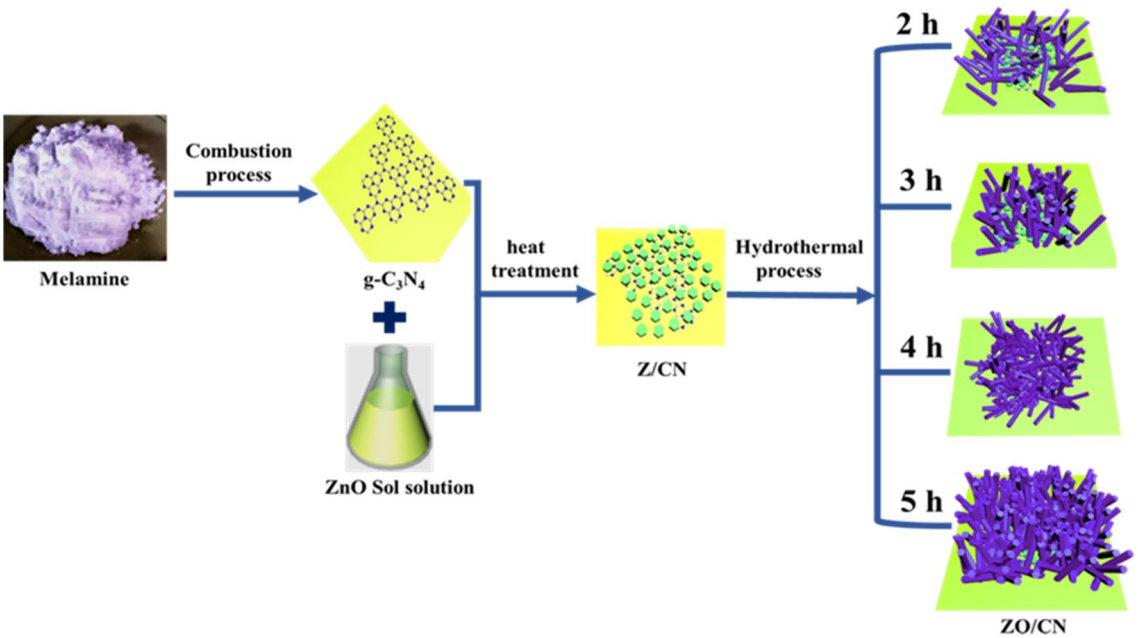

Fig. 1 The preparation flowchart of the ZO/CN series samples

with a diameter of 1 cm and a depth of 2 mm in the center of the surface, no filter, other parameters could not be further found. The UV–Vis diffuse reflectance spectrum (UV–Vis, PE Lambda 1050, PerkinElmer), and an X-ray photoelectron spectroscopy (XPS, ThermoFisher Scientific) was used to further study the surface chemical composition and element states of the samples.

3 Results and discussion

Figure. 2 shows the XRD patterns of the CN and ZO/CN composite samples. In the CN sample, corresponding to the (100) and (002) diffraction planes of g-C_3N_4 (marked as "▼"), two distinct characteristic peaks are obvious at 13.0° and 27.3° of 2θ [26], which are attributed to the in-plane structural packing motif of tri-s-triazine units and the interplanar stacking of aromatic systems in the sample. The peaks at the 2θ of 31.7 °, 34.3 °, 36.2 °, 47.5 °, 56.5, 62.8 °, 66.3 °, 67.9 ° and 69.0 ° in the ZO/CN series composite samples correspond to the (100), (002), (101), (102), (110), (103), (200), (112) and (201) diffraction planes of the hexagonal wurtzite structure ZnO (marked as "♦", JCPDS No. 36–1451) [27], respectively. And the peak at the 2θ of 27.3 ° appearing in all the ZO/CN series samples correspond to g-C_3N_4 (002) plane, which indicates the successful synthesis of the composites. There are no visible ZnO related diffraction peaks in the ZCN sample shown in Fig. 2a, but the corresponding weak intensity peaks can be observed in the insert of Fig. 2a (The insert is a local enlargement of Fig. 2a), indicating that the amount of crystalline ZnO is very less, which may be because the total amount of ZnO is small, or ZnO is present in the form of extremely fine nanocrystals or amorphous. However, with the increase of the hydrothermal time, the characteristic peak intensity of the wurtzite ZnO in the ZO/CN series samples changes regularly. The ZO/CN-2 sample with the shortest hydrothermal time of 2 h shows the highest intensity of the ZnO characteristic peaks which is mainly attributed to the ZnO seed layer on the surface of the g-C_3N_4 considering the sparse ZnO nanorods in the composite, as shown in the SEM image in Fig. 3b, c, while the ZO/CN-3 sample with more ZnO nanorods shows the lowest XRD diffraction peak intensity associated with ZnO. These data show that randomly oriented polycrystalline ZnO was rapidly generated in the composite samples in the initial stage of the reaction. The highest peak intensity of the ZO/CN-2 sample in the composite samples is attributed to the formation of randomly oriented ZnO particles with good crystallization after hydrothermal time of 2 h. As the hydrothermal reaction proceeded, crystal surface energy became the main driving force affecting the morphology of ZnO product, and ZnO crystal began to grow preferentially along the low-energy (002) surface. At the same time, the ZnO seed layer began to dissolve under hydrothermal conditions. The two processes occurred simultaneously during the hydrothermal process, namely, the dissolution of small size ZnO seed particle and the growth of ZnO nanorods. With the further increase of hydrothermal time, the ZnO characteristic peak intensity in the ZO/CN-4 and ZO/CN-5 samples increases gradually. The results indicate that the number of ZnO nanorods increases with hydrothermal time, and which is confirmed by the following SEM measurements. Compared

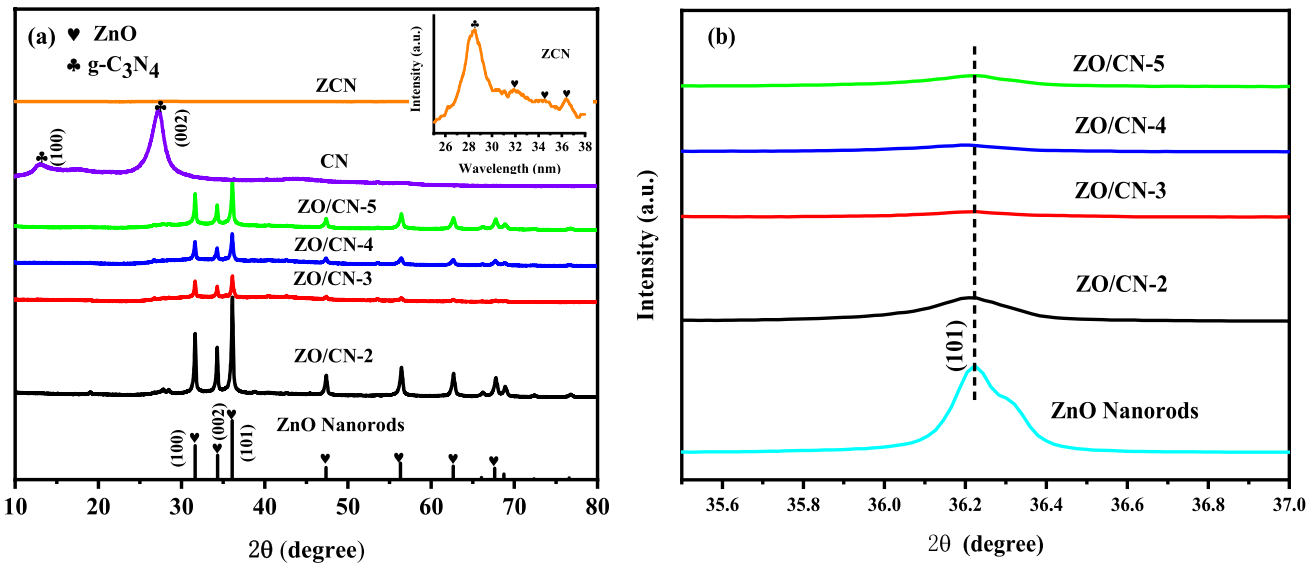

Fig. 2 **a** The XRD diffraction patterns of the ZnO nanorods, CN and ZO/CN series samples (The insert is a local enlargement of the ZCN sample pattern) and **b** The local enlargement of the XRD patterns of the ZnO and ZO/CN series samples

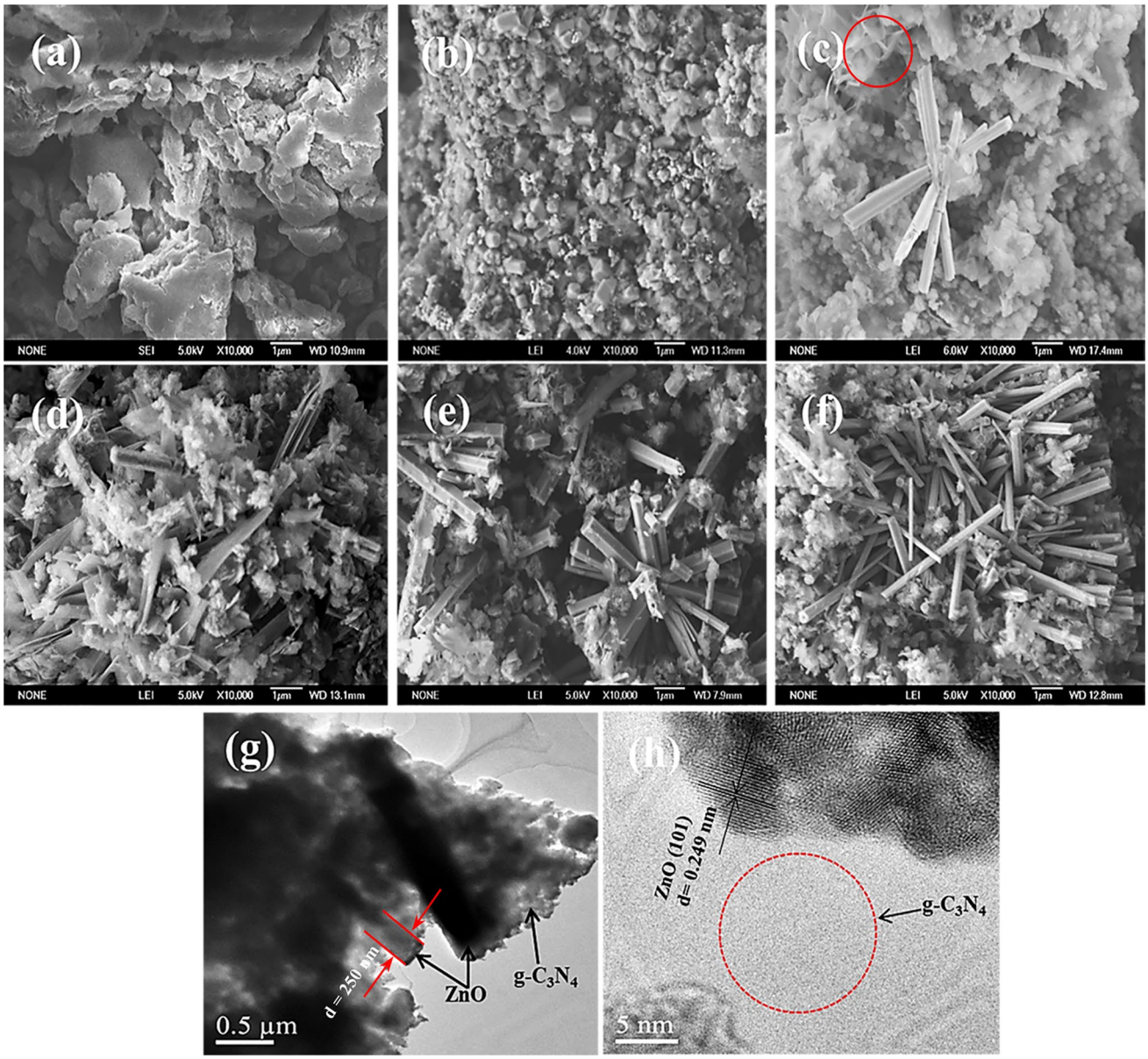

Fig. 3 The SEM images of the **a** CN, **b** Z/CN, **c** Z/CN-2, **d** Z/CN-3, **e** Z/CN-4 and **f** Z/CN-5 samples, and the **g**, **h** TEM images of the ZO/CN-3 sample

with the CN sample, the (100) and (002) characteristic peaks of g-C_3N_4 in all the composite samples become very weak, which is due to the significant change of g-C_3N_4 crystalline structure during hydrothermal process. The result is confirmed by the following SEM and TEM measurements in Fig. 3. It can be seen that the microstructure of g-C_3N_4 was damaged with the increase of hydrothermal time, and its size changed from micron scale to nanometer scale. The decrease of structure size widens the XRD characteristic peak. There are no other peaks in the XRD patterns of the composite samples, indicating that no impurities were formed in the hydrothermal process. Figure 2b shows a local enlargement of the ZnO (101) diffraction peak of the ZO/CN-2 sample, from which it can be seen that the ZnO (101) peak shifts slightly to the direction of small angle. The peak shift may be attributed to lattice parameter change, residual stress and stacking fault density.

The surface morphology of the CN and ZO/CN series samples was investigated with SEM and TEM, as shown in Fig. 3. Figure 3a shows the irregular bulk morphology of the CN sample and Fig. 3b shows the morphology of the Z/CN sample with ZnO seed particles deposited on the surface of the bulk g-C_3N_4. The average size of ZnO seed crystals is between 20 and 50 nm. Figure 3 (c-f) shows the

images of the ZO/CN series samples, in which it can be clearly seen that the ZnO nanorods with regular hexagonal prism shape grew outward from the center of the seed particles on the surface of the bulk g-C_3N_4. In the ZO/CN-2 sample grown for 2 h, only a few nanorods surrounded by agglomerated ZnO nanoparticles can be observed in Fig. 3c. However, with the increase of hydrothermal time, more and more nanorods were grown in the composites, as indicated by the ZO/CN-3, ZO/CN-4 and ZO/CN-5 samples in Fig. 3d–f. With the increase of hydrothermal time, the diameter of ZnO nanorods decreases but the length increases. The aspect ratio of ZnO nanorods changes from 6:1 for hydrothermal of 2 h to 8:1 for hydrothermal of 5 h. In addition, as shown in Fig. 3a–f, compared with the bulk g-C_3N_4, the bulk g-C_3N_4 structure gradually transforms into clustered nanoflakes with the increase of hydrothermal time in the ZO/CN-X series samples. As shown in the red circle in Fig. 3c, the size of g-C_3N_4 also shows a tendency to change from micrometer scale to nanometer scale. In addition, a large number of agglomerated ZnO seed particles in the ZO/CN-2 sample gradually decreases with hydrothermal time, and almost disappeared in the ZO/CN-5 sample. Moreover, the coexistence of g-C_3N_4 and ZnO nanorods in the composite samples is further confirmed by the TEM measurements of the ZO/CN-3 sample in Fig. 3g, h, in which the 0.249 nm plane spacing corresponds to the (101) planes of the hexagonal ZnO.

The element composition of the ZO/CN-3 sample is identified by the EDXS analysis in Fig. 4. Figure 4a shows the scanning area of the sample, and the peaks in Fig. 4 (b) indicate the C, N, O and Zn elements in the ZO/CN-3 sample, respectively.

The binding states of the elements in the ZO/CN-3 composite sample were examined by the XPS measurements, as shown in Fig. 5. Figure 5a shows the electron binding states in C 1 s, N 1 s, O 1 s and Zn 2p orbitals in the composite sample, in which the C and N elements are from g-C_3N_4, and the Zn and O elements are from ZnO in the composite, respectively. The C 1 s electron binding state shows two peaks of 284.7 eV and 288.4 eV in Fig. 5b, corresponding to the C–C bond and sp^2-bonded aromatic ring (N = C-N) of g-C_3N_4, respectively [28, 29]. The N 1 s electron binding state peak can be fitted into three peaks with the centers of 398.9 eV, 399.9 eV and 400.2 eV, as shown in Fig. 5c, in which the peak at 398.9 eV is attributed to the sp^2-bonded carbon triazine rings (C = N–C) in the ring structure, and the peaks at 399.9 eV and 400.2 eV are attributed to the tertiary nitrogen bonded to carbon atoms (N-$(C)_3$) and amino groups (C-N-$(H)_2$), respectively [30, 31]. Figure 5d shows the O 1 s electron binding state in the ZO/CN-3 sample, in which the O 1 s binding energy can also be fitted into three peaks of 530.15 eV, 531.27 eV and 532.49 eV, corresponding to the lattice oxygen of ZnO (O^{2-} ions), V_O defects and chemisorbed oxygen (H_2O, O_2, OH^-, etc.), respectively. And Fig. 5e shows the Zn 2p electron binding state in the sample, and two characteristic peaks at 1021.97 eV and 1045.10 eV correspond to the Zn $2p_{3/2}$ and Zn $2p_{1/2}$ states, respectively [32], indicating that the oxidation state of Zn in the ZO/CN-3 sample is + 2 [33]. The XPS results confirm the successful synthesis of the ZO/CN composite sample.

The UV–Vis diffuse reflectance absorption spectra of the g-C_3N_4 and Zn/CN series composite samples are shown in Fig. 6. The absorption edge of the CN sample is about 470 nm and that of the ZO/CN series samples are about 400 nm, which indicates the intrinsic absorption of g-C_3N_4

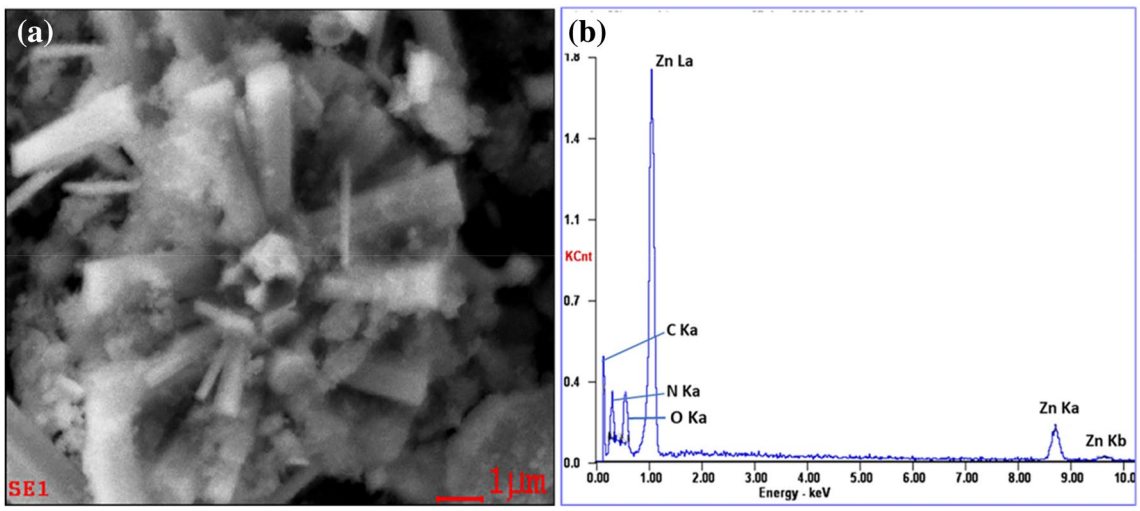

Fig. 4 The EDXS measurement of the ZO/CN-3 sample: **a** The scanning area of the ZO/CN-3 sample for element mapping and **b** The detailed element composition

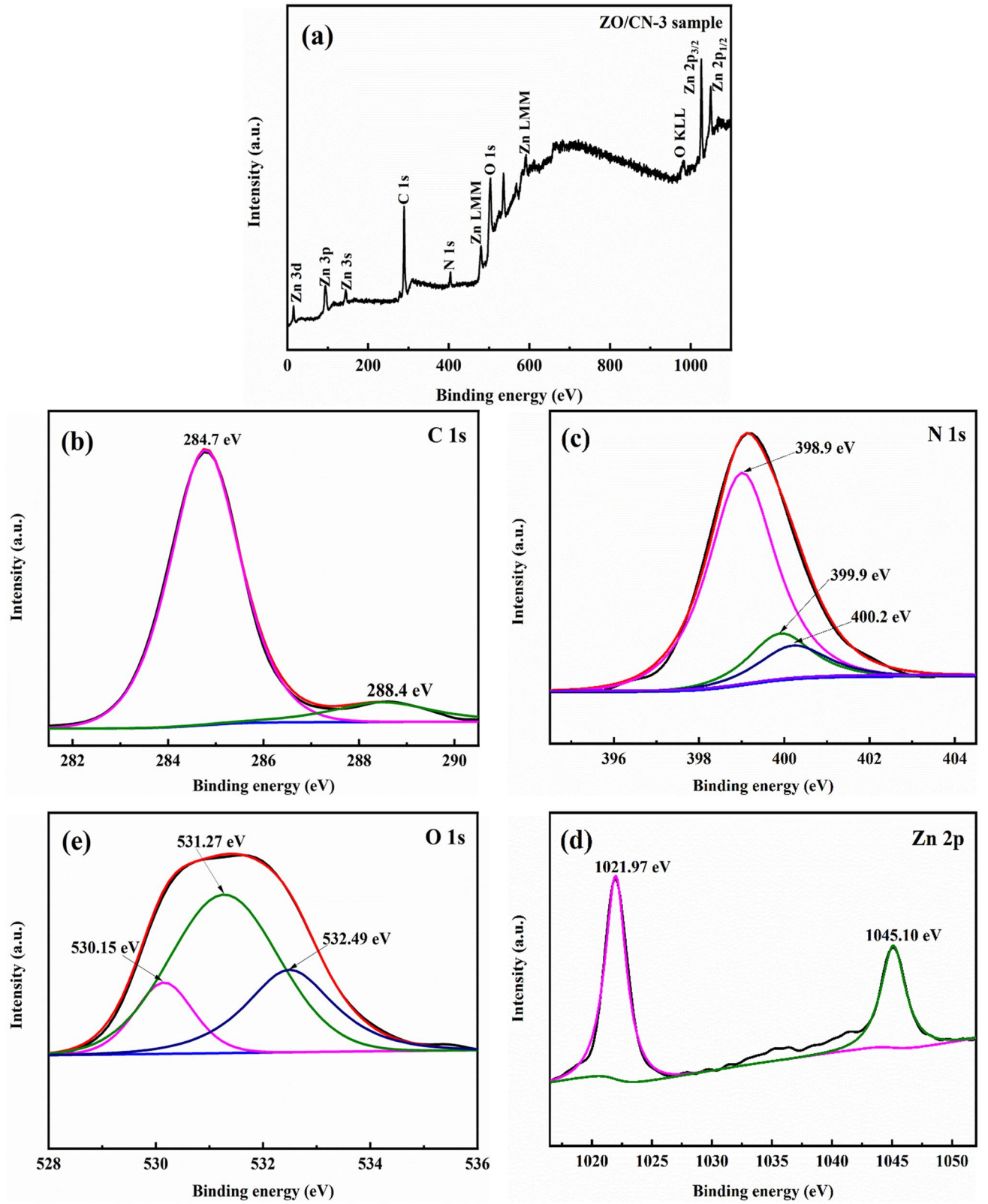

Fig. 5 The XPS spectra of the ZO/CN-3 sample: **a** The full spectrum, **b**–**e** The binding energy of C 1 s, N 1 s, O 1 s, and Zn 2p, respectively

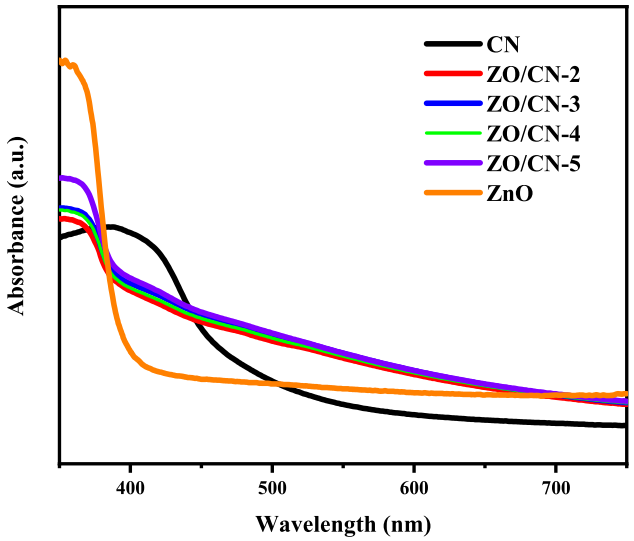

Fig. 6 The UV–Vis diffuse reflectance absorption spectra of the ZnO, CN and ZO/CN series samples

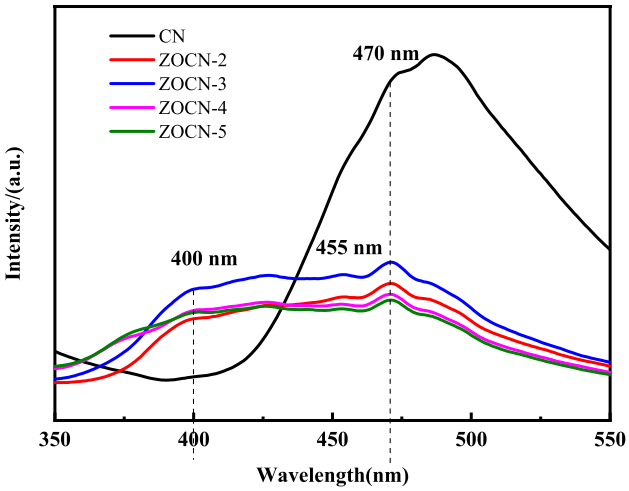

Fig. 7 The PL spectra of CN, ZO/CN-2, ZO/CN-3, ZO/CN-4 and ZO/CN-5 samples were studied at the emission wavelength of 300 nm

and ZnO, respectively [34]. With the increase of hydrothermal time, the intrinsic absorption of the ZO/CN series samples increases gradually in the UV region, which is due to the synergistic effect of the dissolution of ZnO seed particles and the growth of ZnO nanorods. The lowest absorbance of the ZO/CN-2 sample among the composites samples in the UV region is dominated by the ZnO seed particles, while the highest absorbance of the ZO/CN-5 sample is determined by the dense ZnO nanorods. The absorbance of the ZO/CN-3 and ZO/CN-4 samples with similar value is between that of the ZO/CN-2 and ZO/CN-5 due to the synergistic effect. Furthermore, the visible light absorption of the ZO/CN series composite samples is higher than that of the CN samples at the wavelength higher than 475 nm. Considering that the wavelength higher than the intrinsic absorption of ZnO and g-C_3N_4, the strong absorption of the composite samples should be attributed to the diffuse reflection of light between the dense ZnO nanorods, which is favorable for the samples to utilize sunlight.

Figure 7 shows the PL spectra of the CN and ZO/CN series composite samples excited by a wavelength of 300 nm. There are two peaks at 470 nm and 400 nm in ZO/ CN-x sample, in which two peaks indicate the intrinsic emissions of g-C_3N_4 and ZnO, respectively [11, 35]. Among all the samples, the intrinsic emission peak intensity of g-C_3N_4 in the CN sample is the highest, while in the composite samples, it decreases with the extension of hydrothermal time due to the gradual increase of the number of ZnO nanorods. Interestingly, although numerous of ZnO seed particles are confirmed in the ZO/CN-2 sample by the SEM and XRD measurements, the intrinsic emission peak intensity of ZnO is the lowest in the composite samples, which is attributed to the high separation efficiency of the photogenerated electron–hole pairs due to the large contact interface area between ZnO seed particles and bulk g-C_3N_4. Furthermore, the relative high V_O defect concentration also contributes to the separation efficiency, which is indicated by the weak peak at 455 nm in the PL measurements. As discussed above, the hydrothermal process actually includes two processes: the dissolution of small size ZnO seed particles and the growth of ZnO nanorods. Considering that the seed particles exist in all the samples, the dissolution of seed particles reduces the amount of photogenerated carriers in ZnO near the interface between two components. The contribution of these two processes makes the intrinsic emission peak intensity of the ZO/CN-3 sample the highest. From the previous SEM measurements, with the increase of hydrothermal time, the number of ZnO nanorods increases in the composite samples. If only ZnO nanorods are considered, the intrinsic emission peak intensity of ZnO in the ZO/CN-4 and ZO/CN-5 samples should be higher than that in the ZO/CN-3 sample. However, as shown in Fig. 7, the intrinsic emission peak intensity of ZnO in the ZO/CN-4 and ZO/CN-5 samples is lower than that in the ZO/CN-3 sample. Therefore, the reduced ZnO intrinsic emission peak intensity in the ZO/CN-4 and ZO/CN-5 samples should be attributed to the separation of photogenerated carriers. Due to the potential difference between g-C_3N_4 and ZnO energy bands, photogenerated holes in ZnO component are transferred to g-C_3N_4 component, which inhibits the recombination of photogenerated electrons and holes in ZnO. Thus, the intrinsic emission peak intensity in the ZO/CN-4 and ZO/CN-5 samples is reduced.

The photocatalytic properties of the CN and ZO-CN series samples were tested by the degradation of MO solution under the simulated sunlight irradiation, as shown in

Fig. 8. Figure 8a, b shows the photocatalytic degradation performance of the samples to MO dye solution, and Fig. 8c shows the cyclic degradation tests of the ZO/CN-3 sample to MO solution to investigate its reusability in photocatalysis. The photocatalytic performance of the composite samples is a combination of specific surface area, nanostructure size, carrier concentration and mobility in crystals and separation efficiency of electron–hole pairs. During the photocatalytic process, the degradation performance of the composite samples at different stages is dominated by different factors. As seen in the figure, the photocatalytic performance of the CN sample is always the lowest because it is actually a single substance of g-C_3N_4, while for the composite samples, the photocatalytic efficiency in the first five minutes follows an order of $E_{ZO/CN-5} > E_{ZO/CN-2} > E_{ZO/CN-3} > E_{ZO/CN-4}$. Considering the dense ZnO nanorods with high aspect ratio grown on the surface of bulk g-C_3N_4, the ZO/CN-5 sample has a large specific area from the ZnO nanorods, then the highest degradation efficiency mainly originates from the surface reaction, which makes the photocatalytic efficiency of the ZO/CN-5 sample the highest. For the ZO/CN-2 sample with high density of ZnO seed particles on the surface of bulk g-C_3N_4, the sufficient photogenerated carriers in ZnO seed particles and high separation efficiency of photogenerated electron–hole pairs contribute to the improvement of photocatalytic degradation. In addition, the high concentration V_O defects in the sample determined by the PL measurements in Fig. 7 also play the same role. Therefore, the ZO/CN-2 sample also shows excellent photocatalytic degradation performance. In the ZO/CN-3 sample with the reduced ZnO seed particles and continuous growth of ZnO nanorods, the number of photogenerated carrier in ZnO seed particles is reduced. Although the effect of the surface reaction from ZnO nanorods is improved, the effect of the separation of photogenerated carrier is inhibited. As a result of synergy, the photocatalytic performance of the ZO/CN-3 sample is decrease compared with the ZO/CN-2 sample. And due to the same reason, the photocatalytic degradation efficiency of the ZO/CN-4 sample is further decreased. However, the photocatalytic efficiency of the samples changes interesting in the first 10 min of testing. At this stage, due to the heavily dissolved seed particles and depleted surface donor defects, the ZO/CN-5 sample shows the worst photocatalytic degradation efficiency, while the other composite samples show the similar degradation efficiency near 75% under the combined action of the factors. The photocatalytic degradation efficiency of the composite samples reaches a stable state at the degradation time of 30 min and follows an order of $E_{ZO/CN-3} > E_{ZO/CN-2} > E_{ZO/CN-4} > E_{ZO/CN-5}$. At this stage, the ZO/CN-3 sample shows the best photocatalytic degradation efficiency, which is attributed to the effective absorption of incident light by g-C_3N_4 and ZnO components and the effective separation of photogenerated electrons and holes. Compared with the ZO/CN-3 sample, the ZO/CN-2 sample with lower specific surface area can absorb lower incident light, but the excellent separation effect makes it show good photocatalytic efficiency. For the ZO/CN-4 sample, although a large number of photogenerated excitons are produced under light irradiation and separated, the depleted surface V_O defects weaken its photocatalytic degradation ability. Due to the same reason, the ZO/CN-5 sample shows the worst photocatalytic performance. From the above discussion, the separation efficiency of photogenerated electron–hole pairs and the surface V_O defects plays a key role in photocatalytic degradation process of ZnO nanorods/g-C_3N_4 composite and the actual photocatalytic degradation ability of the

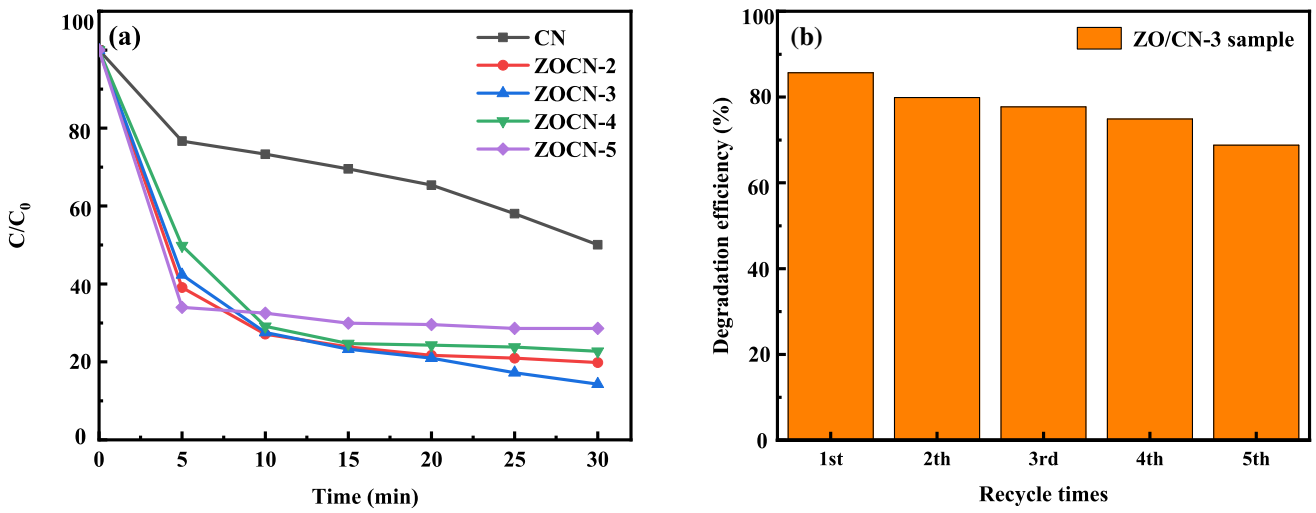

Fig. 8 The photocatalytic degradation performance of the samples to MO solution: **a** The time-dependent photocatalytic degradation efficiency of the samples and **b** Five cyclic photocatalytic degradation tests of the ZO/CN-3 sample

composite sample depends on the synergy of two factors. In short, the bulk g-C_3N_4 with ZnO seed particles sample shows good separation efficiency of photogenerated carriers but low visible light absorbance due to the small specific area. With the increase of hydrothermal time, the dissolution of seed particles reduces photogenerated carrier separation efficiency but the growth of ZnO nanorods improves the ability of visible light absorption and surface reaction. Hence the ZO/CN-3 sample with the hydrothermal time of 3 h shows the best photocatalytic performance. In addition, the growth of ZnO in composite improve the specific area of composite sample and makes the concentration of the degraded solution quickly close to the final concentration.

In fact, the reusability of catalyst is also an important index to evaluate its catalytic performance. In order to investigate the reusability of the composite samples in photocatalysis, the ZO/CN-3 sample was selected for five cycles of photocatalytic degradation to MO solution, as shown in Fig. 8c. Due to the photocorrosion of the composite and the inevitable sample recovery loss in the cyclic photocatalytic test, the photocatalytic degradation efficiency of the ZO/CN-3 sample decreases from 85.7% in the initial test to 68.8% in the fifth test, maintaining good degradation performance. The cyclic photocatalytic degradation test results show that the ZnO nanorods/g-C_3N_4 composite exhibits good reusability in photocatalysis.

In order to determine the mechanism of photocatalytic degradation of the composite samples to MO solution and the main active reaction groups in the process, the ZO/CN-3 sample was selected for the free radical trapping experiment. Triethanolamine (TEOA), isopropanol (IPA) and benzoquinone (BZQ) were selected as the active group scavengers for hole (h^+), hydroxyl radical (•OH) and superoxide anion ($\bullet O_2^-$), respectively. As indicated in Fig. 9, the photocatalytic degradation efficiency of the ZO/CN-3 sample to MO solution is 85.7% in the reaction system without scavenger. When TEOA, BZQ and IPA were added into the reaction system, respectively, the degradation efficiency decreased to 30.9%, 50.9% and 76.6%, indicating that h^+ and $\bullet O_2^-$ are the main active groups in the photocatalytic degradation process, and the contribution of •OH to degradation efficiency is minor. Due to the formation of ZnO Nanorods/g-C_3N_4 heterojunction, the electrons enriched in ZnO conduction band react with the surface absorbed O_2 molecules to generate $\bullet O_2^-$ groups. As the intermediate active groups in photocatalytic reaction process, $\bullet O_2^-$ groups have high activity, and react with other groups to generate •OH groups which directly participate in the degradation reaction of MO molecules.

Based on the above discussion, the separation efficiency of the photogenerated electron–hole pairs is the most important factor affecting the degradation efficiency of ZnO nanorods/g-C_3N_4 composite, then it is necessary to make clear the

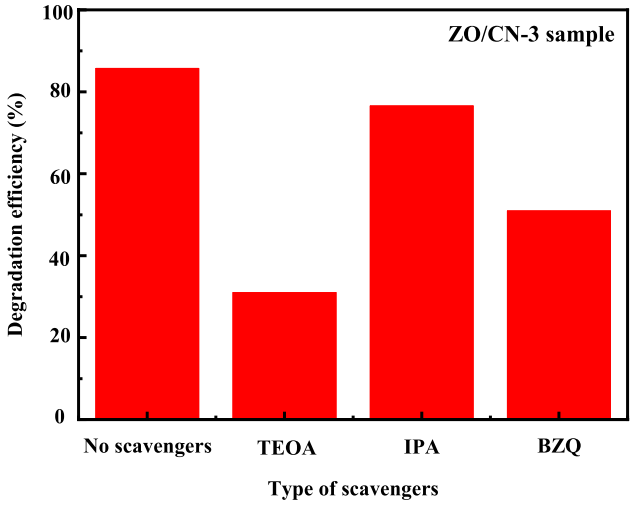

Fig. 9 The contribution comparison of the different scavengers on the degradation efficiency of the ZO/CN-3 sample to MO solution

separation mechanism of the photogenerated electron–hole pairs in photocatalytic degradation process. Considering the conduction band bottom (CB) and valence band top (VB) of g-C_3N_4 are -1.2 eV and + 1.5 eV, respectively, and those of ZnO are -0.5 eV and + 2.87 eV[36,37], the band structure of ZnO nanorods/g-C_3N_4 composite is constructed in Fig. 10. Both ZnO and g-C_3N_4 in the composite are n-type semiconductors, when the composite is irradiated by the light meeting the energy requirements, the electrons in the VBs of the two semiconductors are excited to their respective CBs, leaving holes in their respective VBs. Considering the band potential difference between ZnO and g-C_3N_4, the electrons in the CB of g-C_3N_4 will be transferred to that of ZnO, and the holes in the VB of ZnO would also be transferred to that of g-C_3N_4 at the same time, then the photogenerated electrons and holes in the composite are separated in two different semiconductors. The separation of the photogenerated electron–hole pairs inhibits the recombination of excitons, which prolongs the lifetime of excitons and makes the electrons and holes participate in the photocatalytic degradation reactions effectively. Then the separated electrons react with the O_2 molecules on the surface of ZnO nanorods to generate superoxide anion radicals ($\bullet O_2^-$), and the holes react with the H_2O molecules or hydroxides on the surface of g-C_3N_4 to form hydroxyl radicals (•OH). Finally, $\bullet O_2^-$ and •OH react with MO dye molecules to form the final products. The relevant degradation reactions are described by the following equations:

$$g - C_3N_4 + hv \rightarrow h^+ + e^-\left(g - C_3N_4\right) \quad (2)$$

$$ZnO + hv \rightarrow h^+ + e^-(ZnO) \quad (3)$$

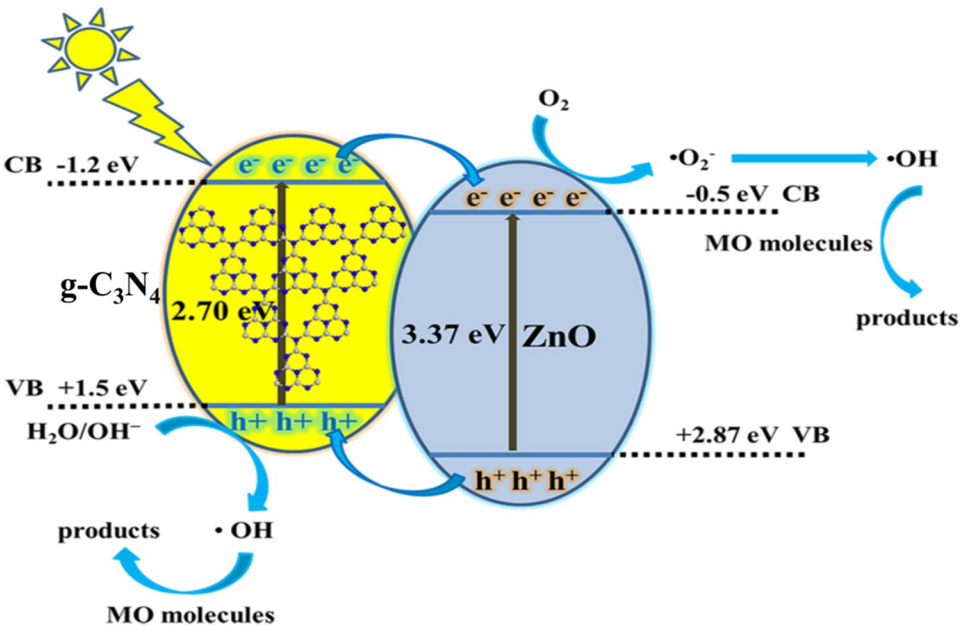

Fig. 10 The schematic diagram of the photocatalytic degradation mechanism of the ZO/CN series samples.

$$e^-\left(g-C_3N_4\right) \rightarrow e^-(ZnO) \quad (4)$$

$$e^-(ZnO) + O_2 \rightarrow \bullet O_2^- \quad (5)$$

$$h^+(ZnO) \rightarrow h^+\left(g-C_3N_4\right) \quad (6)$$

$$h^+\left(g-C_3N_4\right) + H_2O/OH^- \rightarrow \bullet OH \quad (7)$$

$$\bullet O_2^- + H^+ \rightarrow HO_2\bullet \quad (8)$$

$$HO_2\bullet \rightarrow O_2 + H_2O_2 \quad (9)$$

$$H_2O_2 + \bullet O_2^- \rightarrow \bullet OH + OH^- + O_2 \quad (10)$$

$$\bullet OH + MO \rightarrow \text{degradation products} \quad (11)$$

4 Conclusions

ZnO nanorods/g-C_3N_4 composite was prepared by growing ZnO nanorods on the surface of bulk g-C_3N_4 via a hydrothermal method. The composite preparation conditions and the effects of the morphology of ZnO nanorods on the photocatalytic properties of the composite were investigated. The hydrothermal process includes two processes of the dissolution of ZnO seed particles and the growth of ZnO nanorods, and the ratio of ZnO seed particles to ZnO nanorods can be controlled by hydrothermal time. With the short hydrothermal time of 2 h, the ratio of ZnO seed particles to ZnO nanorods is high. Although the separation effect of photogenerated electron–hole pairs is strong due to the large interface area between ZnO seed particles and g-C_3N_4, the number of carriers is insufficient, thus the photocatalytic performance of the composite is poor. While with the long hydrothermal time more than 4 h, the ratio of ZnO seed particles to ZnO nanorods is low due to the dissolution of ZnO seed particles. Although numerous of photogenerated carriers are produced due to the dense ZnO nanorods, the reduced interface area between ZnO and g-C_3N_4 crystals reduces the separation efficiency of the photogenerated electron–hole pairs, and the recombination of excitons also leads to the poor photocatalytic degradation efficiency of the composite. While for the sample prepared with 3 h of hydrothermal time, the sufficient photogenerated carriers and the good photogenerated electron–hole pair separation efficiency makes the composite sample show the best photocatalytic performance, in which the main active factors contributing to the photocatalytic degradation efficiency are holes and superoxide groups. In our research work, the growth of ZnO nanorods/g-C_3N_4 composites can be well controlled by adjusting the hydrothermal holding time under a certain hydrothermal temperature, and the microstructure can be further adjusted. That is to say, the separation efficiency of photogenerated electron–hole pairs in the composite can be indirectly controlled by material design, which provides a reference for the design of ZnO nanorods/g-C_3N_4 related photocatalytic composites.

Acknowledgements This work was financially supported by the Entrustment of Scientific and Technological Projects by Chinese Enterprises and Institutions (LZSN-KJ-002, 2018040-G, ky2019047) and the Hubei Provincial Department of Education (B2018058).

Declarations

Conflicts of interest There are no conflicts of interest to declare.

References

1. L. Li, M. Mao, X. She, J. Yi, M. He, L. Pan, Z. Chen, H. Xu, H. Li, Direct Z-scheme photocatalyst for efficient water pollutant degradation: A case study of 2D g-C_3N_4/$BiVO_4$. Mater. Chem. Phys. **241**, 122308 (2020)
2. J. Yi, H. Li, Y. Gong, X. She, Y. Song, Xu. Yuanguo, J. Deng, S. Yuan, Xu. Hui, H. Li, Phase and interlayer effect of transition metal dichalcogenide cocatalyst toward photocatalytic hydrogen evolution: the case of $MoSe_2$. Appl. Catal. B **243**, 330–336 (2019)
3. H. Heidarpour, M. Padervand, M. Soltanieh, M. Vossoughi, Enhanced decolorization of rhodamine B solution through simultaneous photocatalysis and persulfate activation over Fe/C_3N_4 photocatalyst. Chem. Eng. Res. Des. **153**, 709–720 (2020)
4. B. Gerislioglu, A. Ahmadivand, J. Adam, Infrared plasmonic photodetectors: the emergence of high photon yield toroidal metadevices. Mater. Today Chem. **14**, 100206 (2019)
5. X. Li, K. Zhang, M. Zhou, K. Yang, S. Yang, X. Ma, Yu. Changlin, Yu. Xie, W. Huang, Q. Fan, A novel approach to synthesize nitrogen-deficient g-c_3n_4 for the enhanced photocatalytic contaminant degradation and electrocatalytic hydrogen evolution. NANO **15**, 2050006 (2020)
6. V. Kumaravel, S. Mathew, J. Bartlett, S.C. Pillai, Photocatalytic hydrogen production using metal doped TiO_2: A review of recent advances. Appl. Catalysis B Environ. **244**, 1021–1064 (2019)
7. R. He, H. Liang, C. Li, J. Bai, Enhanced photocatalytic hydrogen production over Co_3O_4@g-C_3N_4 p-n junction adhering on one-dimensional carbon fiber. Coll. Surf. A **586**, 124200 (2020)
8. X. Wang, K. Maeda, A. Thomas, K. Takanabe, G. Xin, J.M. Carlsson, K. Domen, M. Antonietti, A metal-free polymeric photocatalyst for hydrogen production from water under visible light. Nature Mater. **8,** 76–80 (2009)
9. Y. Wang, S. Zhao, Y. Zhang, J. Fang, W. Chen, S. Yuan, Y. Zhou, Facile synthesis of self-assembled g-C_3N_4 with abundant nitrogen defects for photocatalytic hydrogen evolution. ACS Sustain. Chem. Eng. **6**, 10200–10210 (2018)
10. J. Zhu, P. Xiao, H. Li, S.A. Carabineiro, Graphitic carbon nitride: synthesis, properties, and applications in catalysis. ACS Appl Mater Interfaces **6**, 16449–16465 (2014)
11. J. Jiang, Mu. Zhao, H. Xing, Wu. Qiannan, X. Yue, Y. Lin, Insights into the synergetic effect for enhanced UV/visible-light activated photodegradation activity via Cu-ZnO photocatalyst. Appl. Surf. Sci. **478**, 1037–1045 (2019)
12. Yu. Fucheng, D. Nan, B. Wang, Z. Liu, Y. Li, L. He, X. Tang, J. Zhang, Catalytic properties of the composite of La-doped ZnO nanorods and Ag_2CrO_4 nanoparticles. Appl. Phys. A **126**, 482 (2020)
13. T. Huang, W. Zhang, S. Pan, L. Shi, J. Zhu, X. Wang, Fu. Yongsheng, General synthesis strategy for hollow porous prismatic graphitic carbon nitride: a high-performance photocatalyst for H_2 production and degradation of RhB. J. Mater. Sci. **55**, 6037–6050 (2020)
14. W. Luo, X. Chen, Z. Wei, D. Liu, W. Yao, Y. Zhu. Three-dimensional network structure assembled by g-C3N4 nanorods for improving visible-light photocatalytic performance. Appl. Catalysis B Environ. **255**, 117761 (2019)
15. Y. Si, Z. Sun, L. Huang, M. Chen, Wu. Limin, A "ship-in-a-bottle" strategy to fabricate highly crystallized nanoporous g-C_3N_4 microspheres under pressurized conditions. J. Mater. Chem. A **7**, 8952–8959 (2019)
16. Z. Zhu, F. Zhou, S. Zhan, Enhanced antifouling property of fluorocarbon resin coating (PEVE) by the modification of g-C_3N_4/Ag_2WO_4 composite step-scheme photocatalyst. Appl. Surf. Sci. **506**, 144934 (2020)
17. R. Zhang, S. Niu, X. Zhang, Z. Jiang, J. Zheng, C. Guo, Combination of experimental and theoretical investigation on Ti-doped g-C_3N_4 with improved photo-catalytic activity. Appl. Surf. Sci. **489**, 427–434 (2019)
18. Y. Cui, H. Wang, C. Yang, M. Li, Y. Zhao, F. Chen, Post-activation of in situ B-F codoped g-C_3N_4 for enhanced photocatalytic H_2 evolution. Appl. Surf. Sci. **441**, 621–630 (2018)
19. Z. Ren, F. Chen, K. Wen, J. Lu. Enhanced photocatalytic activity for tetracyclines degradation with Ag modified g-C_3N_4 composite under visible light. J. Photochem. Photobiol. A Chem. **389**, 112217 (2020)
20. D. Zhu, S. Liu, M. Chen, J. Zhang, X. Wang, Flower-like-flake Fe_3O_4/g-C_3N_4 nanocomposite: facial synthesis, characterization, and enhanced photocatalytic performance. Colloids Surf., A **537**, 372–382 (2018)
21. R. Zhang, K. Huang, H. Wei, D. Wang, Ou. Gang, N. Hussain, Z. Huang, C. Zhang, Wu. Hui, Ultra-low-temperature growth of CdS quantum dots on g-C_3N_4 nanosheets and their photocatalytic performance. Dalton Trans **47**, 1417–1421 (2018)
22. S. Zuo, Xu. Haiming, W. Liao, X. Yuan, L. Sun, Q. Li, J. Zan, D. Li, D. Xia, Molten-salt synthesis of g-C_3N_4-Cu_2O heterojunctions with highly enhanced photocatalytic performance. Colloids Surf. A **546**, 307–315 (2018)
23. P. Yang, J. Wang, G. Yue, R. Yang, P. Zhao, L. Yang, X. Zhao, D. Astruc. Constructing mesoporous g-C_3N_4/ZnO nanosheets catalyst for enhanced visible-light driven photocatalytic activity. J. Photochem. Photobiol. A Chem. **388**, 112169 (2020)
24. D.R. Paul, S. Gautam, P. Panchal, S.P. Nehra, P. Choudhary, A. Sharma, ZnO-Modified g-C_3N_4: a potential photocatalyst for environmental application. ACS Omega **5**, 3828–3838 (2020)
25. W. Liu, M. Wang, C. Xu, S. Chen, Facile synthesis of g-C_3N_4/ZnO composite with enhanced visible light photooxidation and photoreduction properties. Chem. Eng. J. **209**, 386–393 (2012)
26. S.W. Zhao, M. Zheng, H.L. Sun, S.J. Li, Q.J. Pan, Y.R. Guo, Construction of heterostructured g-C_3N_4/ZnO/cellulose and its antibacterial activity: experimental and theoretical investigations. Dalton Trans. **49**, 3723–3734 (2019)
27. N. Ning, Y. Tian, J. Zhang, J. Kong, W. Lingchao, L. Zhao, H. Jianhui . Z-scheme 2D/3D g-C3N4@ZnO with enhanced photocatalytic activity for cephalexin oxidation under solar light. Chem. Eng. J. **352**, 412–422 (2018)
28. A. Abdolhoseinzadeh, S. Sheibani, Enhanced photocatalytic performance of Cu_2O nano-photocatalyst powder modified by ball milling and ZnO. Adv. Powder Technol. **31**, 40–50 (2020)
29. Z. Wang, Y. Huo, Y. Fan, Wu. Rong, Wu. Hao, F. Wang, Xu. Xiaohong, Facile synthesis of carbon-rich g-C_3N_4 by copolymerization of urea and tetracyanoethylene for photocatalytic degradation of Orange II. J. Photochem. Photobiol. A **358**, 61–69 (2018)
30. Q. Ma, Yu. Yuan Fang, J.S. Liu, Fu. Xinghua, H. Li, S. Chu, Y. Chen, Facile synthesis of ZnO morphological evolution with tunable growth habits: Achieving superior gas-sensing properties of hemispherical ZnO/Au heterostructures for trimethylamine. Phys. E **106**, 180–186 (2018)
31. N. Abdel Aal, F. Al-Hazmi, A.A. Al-Ghamdi, A.A. Al-Ghamdi, F. El-Tantawy, F. Yakuphanoglu. Novel rapid synthesis of zinc oxide nanotubes via hydrothermal technique and antibacterial

properties. Spectrochim. Acta Part A Mol. Biomol. Spectroscopy **135**, 871–877 (2015)
32. X. Chen, R. Shi, Q. Chen, Z. Zhang, W. Jiang, Y. Zhu, T. Zhang, Three-dimensional porous g-C_3N_4 for highly efficient photocatalytic overall water splitting. Nano Energy **59**, 644–650 (2019)
33. Qi. Zhang, X. Zhang, Facile fabrication of phosphorus-doped g-C_3N_4 exhibiting enhanced visible light photocatalytic degradation performance toward textile dye. Solid State Sci. **89**, 150–155 (2019)
34. S. Prabhu, M. Pudukudy, S. Harish, M. Navaneethan, S. Sohila, K. Murugesan, R. Ramesh, Facile construction of djembe-like ZnO and its composite with g-C_3N_4 as a visible-light-driven heterojunction photocatalyst for the degradation of organic dyes. Mater. Sci. Semiconduct. Process. **106**, 104754 (2020)
35. K.C. Verma, R.K. Kotnala, Oxygen vacancy induced by La and Fe into ZnO nanoparticles to modify ferromagnetic ordering. J. Solid State Chem. **237**, 211–218 (2016)
36. Q. Zhong, H. Lan, M. Zhang, H. Zhu, Bu. Ming, Preparation of heterostructure g-C_3N_4/ZnO nanorods for high photocatalytic activity on different pollutants (MB, RhB, Cr(VI) and eosin). Ceram. Int. **46**, 12192–12199 (2020)
37. S. Ma, S. Zhan, Y. Xia, P. Wang, Q. Hou, Q. Zhou, Enhanced photocatalytic bactericidal performance and mechanism with novel Ag/ZnO/g-C_3N_4 composite under visible light. Catal. Today **330**, 179–188 (2019)
38. K. Ravichandran, E. Sindhuja, Fabrication of cost effective g-C_3N_4 + Ag activated ZnO photocatalyst in thin film form for enhanced visible light responsive dye degradation. Mater. Chem. Phys. **221**, 203–215 (2019)
39. X. Lia, M. Li, J. Yang, X. Li, Hu. Tingjing, J. Wang, Y. Sui, Wu. Xingtong, L. Kong, Synergistic effect of efficient adsorption g-C_3N_4/ZnO composite for photocatalytic property. J. Phys. Chem. Solids **75**, 441–446 (2014)